

Axial Strain Calculation Using a Low-Pass Digital Differentiator in Ultrasound Elastography

Jianwen Luo, *Student Member, IEEE*, Jing Bai, *Fellow, IEEE*, Ping He, *Senior Member, IEEE*, and Kui Ying



Abstract—In ultrasound elastography, tissue axial strains are calculated from the gradient of the estimated axial displacements. However, the common differentiation operation amplifies the noises in the displacement estimation, especially at high frequencies. In this paper, a low-pass digital differentiator (LPDD) is proposed to calculate the axial strain from the estimated tissue displacement. Several LPDDs that have been well developed in the field of digital signal processing are presented. The corresponding performances are compared qualitatively and quantitatively in computer simulations and in preliminary phantom and in vitro experiments. The results are consistent with the theoretical analysis of the LPDDs.

I. INTRODUCTION

ULTRASOUND elastography has become a promising method for aiding in clinical diagnosis by quantifying and imaging the elastic properties of biological tissues [1], [2]. To produce a strain image (i.e., elastogram), an external compression is first applied to the tissue. The axial displacements are then estimated, normally using the cross-correlation analysis applied to the pre- and post-compression ultrasonic A-line windows. Finally, the axial strains are calculated as the gradient (derivative) of the axial displacements [1], [2]. Many research efforts have been devoted to the analysis of echo decorrelation due to the applied external compression, and to the improvements of the accuracy of displacements estimation [3]–[6]. The main focus of this paper, however, is on the calculation of local strain from the estimated tissue axial displacements.

The relationship between the strain and displacement can be described as a numerical differentiation process in mathematical theory. In our work, we treat the numerical differentiation process as a digital differentiator (DD), i.e., a differentiation filter. An ideal full-pass DD has a gain that increases linearly with frequency; hence it amplifies high-frequency noises [7]–[10]. Therefore, one would readily choose a low-pass DD (LPDD) rather than a full-pass one [7]–[9]. The main advantage of using an LPDD is its

capability of analyzing the performances of a particular differentiation method from the point of view of digital signal processing [7], [9]. In addition, some existing methods for strain calculation (such as the least-squares strain estimator (LSQSE) [11], the filtering of a point-symmetric ramp function applied to axial displacements [12], the staggered strain estimation method [13], the combination of the differentiation technique and the low-pass filtering or moving average filtering [2], [11], etc.) can be regarded as special kinds of LPDDs. Therefore, the concept of LPDD may unify the numerical differentiation approach for axial strain calculation from estimated axial displacements in ultrasound elastography.

The overall objective of this study is to compare the performances of various LPDDs on axial strain calculation in elastography, and discuss the results to try to provide some suggestions in choosing an LPDD. In this paper we first present some characteristics of the LPDD in theory and compare various LPDDs. Secondly, we give computer simulation results of various LPDDs on elastographic performances. Thirdly, we describe some preliminary experimental results. Finally, we discuss the results and provide some suggestions for future work.

II. THEORY

In this paper, we mainly evaluate the simple DD [9], the Savitzky-Golay DD [7], [14], [15], the optimum DD [9], and the smoothed DD [9]. The expressions of each DD are listed in Table I. The optimum LPDD is obtained by minimizing the square error of the frequency response between the LPDD and the ideal full-pass DD [9]. The SGDD is further divided into the SG-I DD and the SG-II DD based on the order of polynomial fitting. The SG-I DD uses a linear or quadratic parabola fit and the SG-II DD uses a cubic or quartic parabola fit. The smoothed DD is further divided into the smoothed-I DD and the smoothed-II DD. The smoothed-I DD is constructed by combining a moving average filter of length $2M_1 + 1$ and a simple DD of length $2M_2 + 1$, where $M_2 = [M/2]$, $M_1 = M - M_2$, and $[\cdot]$ represents the operator rounded to the nearest integer. The smoothed-II DD is constructed by combining a moving average filter of length $2M - 1$ and a simple DD of length 3. When $M = 1$ or the filter length is 3, the simple DD and the SG-I DD become the same as the three-point central differentiation formula [16].

Manuscript received July 16, 2003; accepted May 7, 2004. This work is supported in part by the National Natural Science Foundation of China (60171039).

J. Luo, J. Bai, and K. Ying are with the Department of Biomedical Engineering, Tsinghua University, Beijing 100084, P. R. China (e-mail: deabj@tsinghua.edu.cn).

P. He is with the Department of Biomedical, Industrial, and Human Factors Engineering, Wright State University, Dayton, OH 45435-0001.

TABLE I
INPUT-OUTPUT RELATION OF SEVERAL LPDDs.

Kind of LPDD	Input-output relation of the LPDD at a filter length of $2M + 1$
The simple DD	$y(n) = \frac{1}{2M} \Delta_M$, where $\Delta_k = x(n+k) - x(n-k)$, the same below.
The Savitzky-Golay DD	$y(n) = \sum_{k=1}^M \frac{3k}{(2M+1)(M+1)(M)} \Delta_k$ (SG-I DD)
DD	$y(n) = \sum_{k=1}^M \frac{25(3M^4 + 6M^3 - 3M + 1)k - 35(3M^2 + 3M - 1)k^3}{(2M+3)(2M+1)(2M-1)(M+2)(M+1)(M)(M-1)} \Delta_k$ ($M \geq 2$) (SG-II DD)
The optimum DD	$y(n) = \frac{1}{2} (0.2595\Delta_1 + 0.3702\Delta_2)$ ($M = 2$), $y(n) = \frac{1}{2} (0.0976\Delta_1 + 0.1666\Delta_2 + 0.1897\Delta_3)$ ($M = 3$), $y(n) = \frac{1}{2} (0.0464\Delta_1 + 0.0846\Delta_2 + 0.1084\Delta_3 + 0.1148\Delta_4)$ ($M = 4$), etc.
The smoothed DD	$y(n) = \sum_{k=1}^M \frac{1}{M(M+1)} \Delta_k$ ($M \geq 2$) (smoothed-I DD)
DD	$y(n) = \frac{1}{2(2M-1)} [\Delta_{M-1} + \Delta_M]$ ($M \geq 2$) (smoothed-II DD)

The frequency response of an LPDD approximates that of the ideal full-pass DD at low frequencies and attenuates at high frequencies. For a given cutoff frequency, the square error of the frequency response between the LPDD and the ideal DD can measure both the closeness of the LPDD and the ideal DD at frequencies lower than the cutoff frequency and the noise elimination at frequencies higher than the cutoff frequency [9]. The optimum cutoff frequency and the corresponding minimum square error of an LPDD can be obtained by minimizing the square error of the frequency response [9]. The optimum cutoff frequency of an LPDD represents its low-pass range to a certain extent.

Assuming that the input signal is contaminated by independent Gaussian white noises (or a weaker condition of uncorrelated and homoscedastic noises), the noise amplification factor of a digital filter is given by the sum of the squares of the filter impulse response [7], [8]. In practice, e.g., in elastography, it may not satisfy the Gaussian noise assumption. However, the noise amplification factor of an LPDD may still characterize its noise amplification effect to some extent.

In the following we study the relationship between the filter length and each of three indices—the minimum square errors, the optimum cutoff frequencies, and the noise amplification factor. Figs. 1 and 2 show the minimum square errors and the optimum cutoff frequencies as a function of the filter length, respectively. As shown in Fig. 1, the minimum square error decreases as the filter length increases for each type of DD. The optimum DD has the smallest minimum error, which is why the filter is called the “optimum” DD. The SG-I DD and the smoothed-I DD have slightly higher minimum errors, fol-

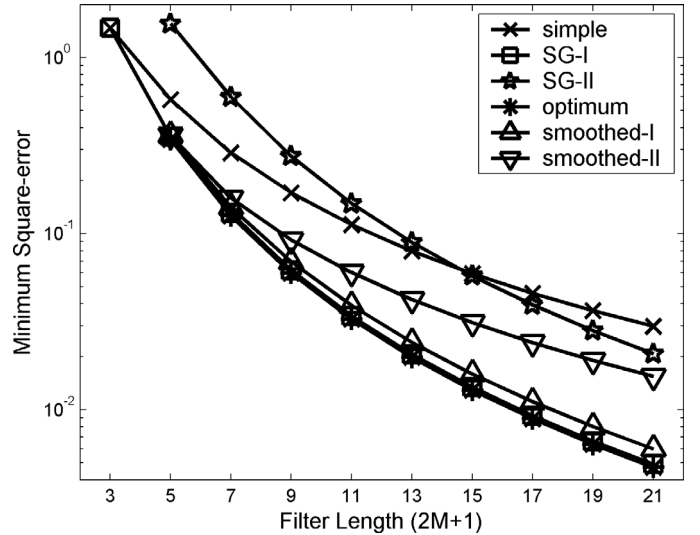


Fig. 1. The minimum square errors of various LPDDs as a function of the filter length. The minimum square errors are plotted on a logarithmic scale.

lowed by the smoothed-II DD, the SG-II DD, and the simple DD. As shown in Fig. 2, the optimum cutoff frequency decreases as the filter length increases. The simple DD has the lowest optimum cutoff frequency while the SG-II DD has the highest optimum cutoff frequency. The optimum cutoff frequencies of the SG-I DD, the optimum DD, and the smoothed-I DD are all close to each other.

According to the Gauss-Markov theorem [17], the SG-I DD can achieve the minimum noise amplification factor. As shown in Fig. 3, the noise amplification factors of the optimum DD and the smoothed-I DD are close to that of

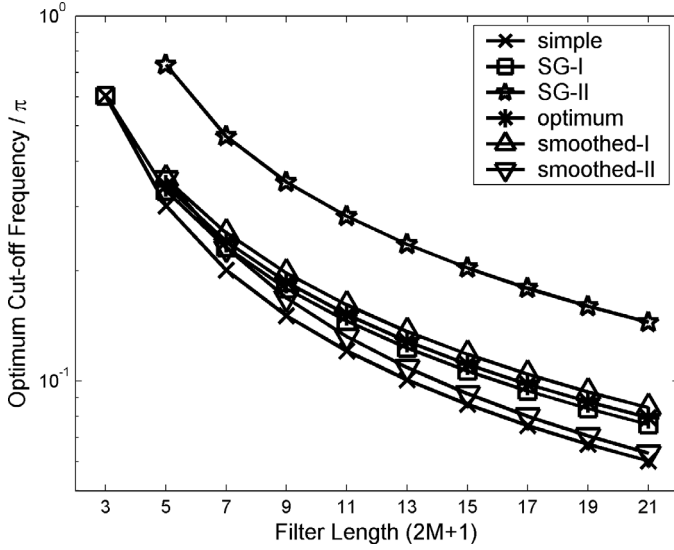


Fig. 2. The optimum cutoff frequencies of various LPDDs as a function of the filter length. The optimum cutoff frequencies are plotted on a logarithmic scale.

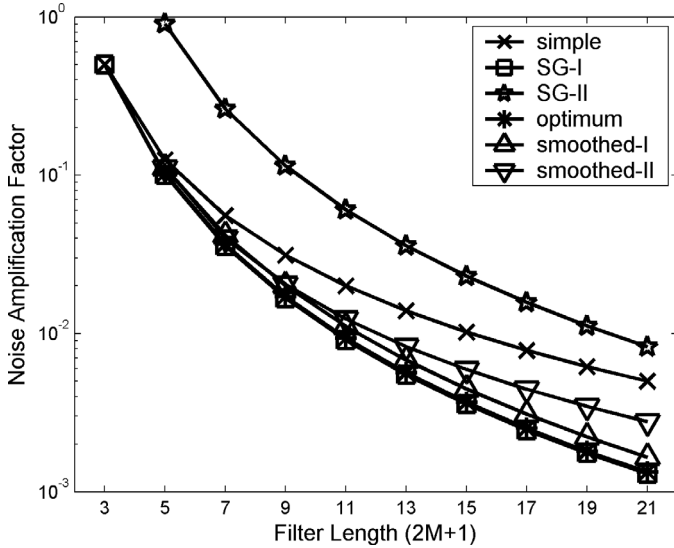


Fig. 3. The noise amplification factors of various LPDDs as a function of the filter length. The noise amplification factors are plotted on a logarithmic scale.

the SG-I DD. The SG-II DD has the highest noise amplification factor.

III. SIMULATION

A. Method

Three indices are used to evaluate the elastographic performances of LPDDs by Monte Carlo simulations in MATLAB 6.5 (The MathWorks Inc., Natick, MA). The indices are elastographic signal-to-noise ratio (SNRe), elastographic contrast-to-noise ratio (CNRe), and elastographic axial resolution. Three models are used in our work—uniform model, single-lesion model, and double-

lesion model. For each model, one type of tissue is simulated. In the uniform model, the tissue is modeled as a homogeneous and anisotropic elastic medium of $50 \times 50 \text{ mm}^2$. The model is used to study the SNRe. In the single-lesion model, the tissue is modeled with a hard circular lesion (inclusion) embedded near the center of a uniform medium of $50 \times 50 \text{ mm}^2$. The lesion has a diameter of 10 mm and is 5 times harder than the background tissue. The model is used to study the CNRe. In the double-lesion model, the tissue has two stiff circular lesions with the same lesion/background contrast placed axisymmetrically in the center of the homogeneous tissue (depth = 60 mm, width = 50 mm). The two lesions are 10 mm in diameter and 5 times harder than the surrounding tissue. The model is used to study the elastographic axial resolution. All three simulated tissues are almost incompressible, with a Poisson's ratio of 0.495. The speed of sound in tissue is assumed to be constant at 1540 m/s. The tissue is assumed to be in a plane strain state, and is compressed in the axial direction by a compressor with an infinite width and a perfect slip boundary. The two lateral sides of the tissue are in free boundary condition. The applied strain is 1.0%. The actual axial displacements and axial strains are calculated by the finite element method (FEM) with the commercial software MARC 2003 (MSC Software Corp., Redwood, CA).

The pre- and postcompression A-lines are generated by a 2-D linear scattering model [18]. The axial component of a transducer point spread function (PSF) has a 50% half-power relative bandwidth and a 5 MHz center frequency whereas the lateral PSF component has a full width at half maximum (FWHM) or a beamwidth of 1 mm. The lateral pitch is equal to 0.4 mm. The scattering function consists of uniformly distributed point scatterers with density of 40 scatterers per pulse width, satisfying the requirement for fully developed speckle [19]. The scatterer strengths are randomly distributed over the pulse width. The 2-D PSF is convolved with the scattering function to obtain the precompression A-lines. Similarly, with the FEM, the postcompression scattering function can be calculated to obtain the postcompression A-lines. The sampling frequency is set at 50 MHz. The sonographic signal-to-noise ratio (SNRs) is set at 30 dB by adding other uncorrelated A-lines as additional colored noises to both the pre- and postcompression A-lines [13].

The axial displacements are estimated using a window length of 2 mm and a window separation of 0.5 mm (i.e., at a 75% overlap). The temporal stretching applied to the postcompression A-lines [5], [6] is not employed. After the axial displacements are estimated, various LPDDs are used to calculate the axial strains from the displacements. For an LPDD at a length of $2M + 1$, the first and last M displacement data are skipped in the strain calculation. Consequently, there are two end blank regions in the 1-D strain profiles as well as in the 2-D strain images.

In the following we compare the three indices to evaluate the elastographic performances of each LPDD on the three models mentioned above.

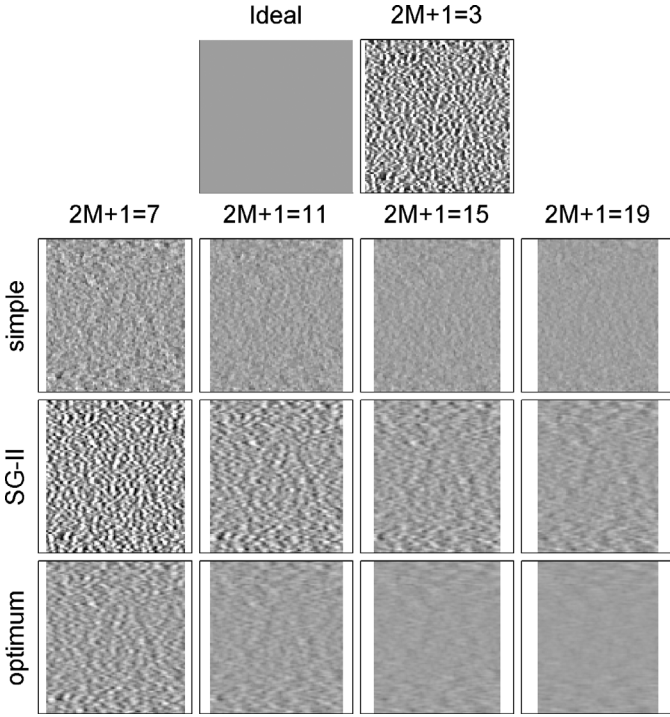


Fig. 4. The ideal axial strain image and strain images obtained by various LPDDs in the homogeneous tissue model. All of the strain images are displayed with the same gray scale range of [0 0.020]. The horizontal axis denotes the axial direction (depth), while the vertical axis denotes the lateral direction (width).

B. Comparison of Signal-to-Noise Ratio

The ideal axial strain image of the uniform model and the strain images calculated by various LPDDs are shown in Fig. 4. The figure shows that the strain image obtained by the simple DD (or SG-I DD) with length of 3 is quite noisy. As the filter length increases, the SNRe seems to be significantly improved. The SNRe of the optimum DD is slightly better than that of the simple DD, while the SNRe of the SG-II DD is the worst.

To compare the SNRes quantitatively, the SNRe is defined as [6]:

$$SNRe = \frac{\mu_s}{\sigma_s}, \quad (1)$$

where μ_s and σ_s are, respectively, the mean and standard deviation of the calculated strains in the homogeneous simulated tissue.

Fig. 5 shows the calculated SNRe of various LPDDs. As the filter length increases, the SNRe of each LPDD is significantly improved. At a low filter length, the SNRes of all the LPDDs except the SG-II DD are almost the same. At a long filter length, however, the SNRes of the optimum DD, the SG-I DD, and the smoothed-I DD are much higher than those of the simple DD and the smoothed-II DD. The SG-II DD has the lowest SNRe at any filter length.

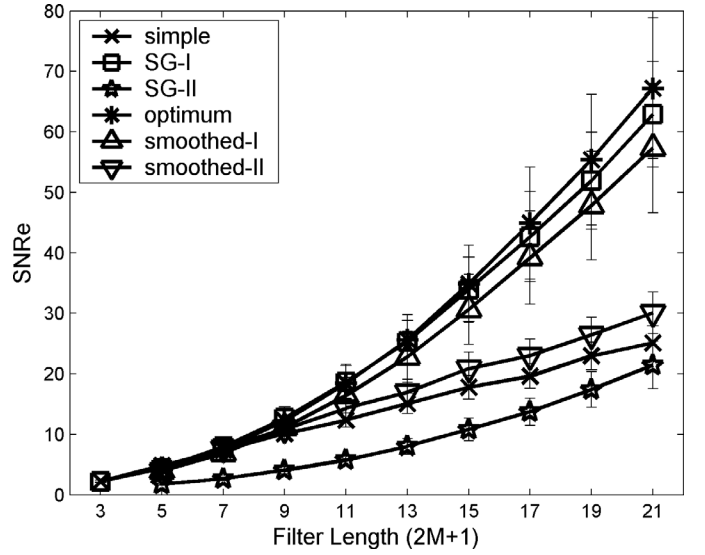


Fig. 5. The SNRes of the strain profiles obtained by various LPDDs. The window length is 2 mm at an overlap of 75%. The SNRe is calculated from a 1-D strain profile on the central line of the tissue. The SNRe on other lateral lines is derated according to the lateral displacements and is not taken into account. The results are the statistical means over 50 independent realizations; the error bars represent the standard deviations.

C. Comparison of Contrast-to-Noise Ratio

The ideal axial strain image of the single-lesion model and the strain images calculated with various LPDDs are shown in Fig. 6. As evident in the figure, the noise performances are quite similar to those in Fig. 4. The contrast between the lesion and the background decreases as the filter length increases. The SG-II appears to have a relatively higher contrast.

The strain contrast in the single-lesion simulated tissue can be calculated by:

$$Ce = \frac{\mu_{sb}}{\mu_{sl}}, \quad (2)$$

where μ_{sb} and μ_{sl} represent the mean values of the strains in the background and the lesion, respectively.

Fig. 7 is a plot of the strain contrast results of various LPDDs. As shown, the contrast decreases as the filter length increases. However, the contrast of the SG-II decreases the least. Its contrast stays the highest, while the simple DD and the smoothed-II DD have the lowest and the second lowest contrast, respectively.

Considering the combined behaviors of the noise and contrast, the CNRe can be used to evaluate the lesion-detection ability. Low noise and high contrast between the lesion and the background contribute a high CNRe, which can increase the ability of detecting lesions. The CNRe can be defined as [20]:

$$CNRe = \frac{2(\mu_{sb} - \mu_{sl})^2}{\sigma_{sb}^2 + \sigma_{sl}^2}, \quad (3)$$

where σ_{sb}^2 and σ_{sl}^2 denote the strain standard deviations in the background tissue and the lesion, respectively.

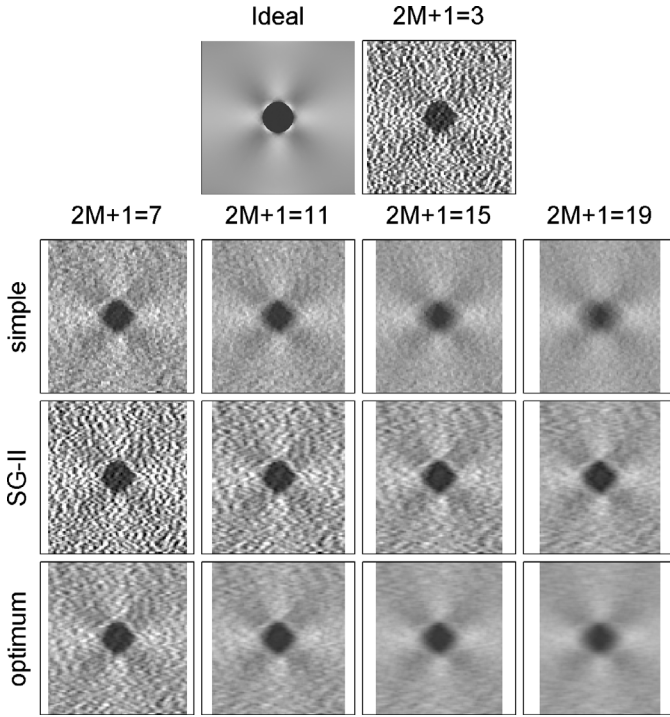


Fig. 6. The ideal axial strain image and strain images obtained by various LPDDs in the one-inclusion tissue model. All of the strain images are displayed with the same gray scale range of [0 0.020]. The horizontal axis denotes the axial direction (depth), while the vertical axis denotes the lateral direction (width).

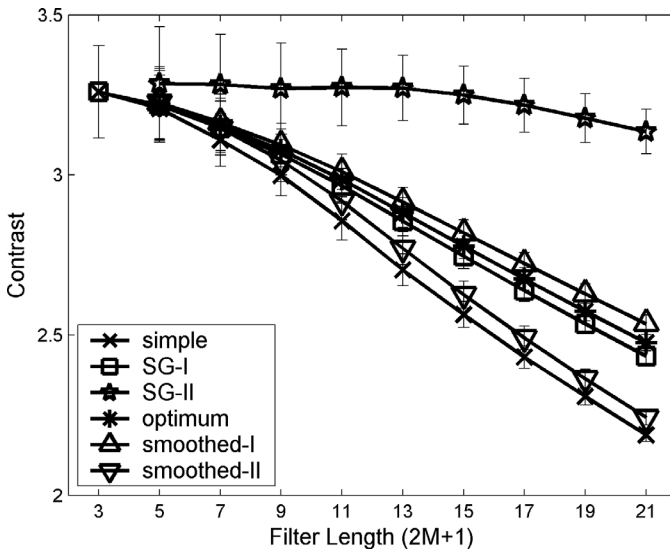


Fig. 7. The contrast of the strain profiles obtained by various LPDDs. The window length is 2 mm at an overlap of 75%. The contrast is calculated from a 1-D strain profile on the central line of the tissue. The results are averaged over 50 independent realizations; the error bars represent the standard deviations.

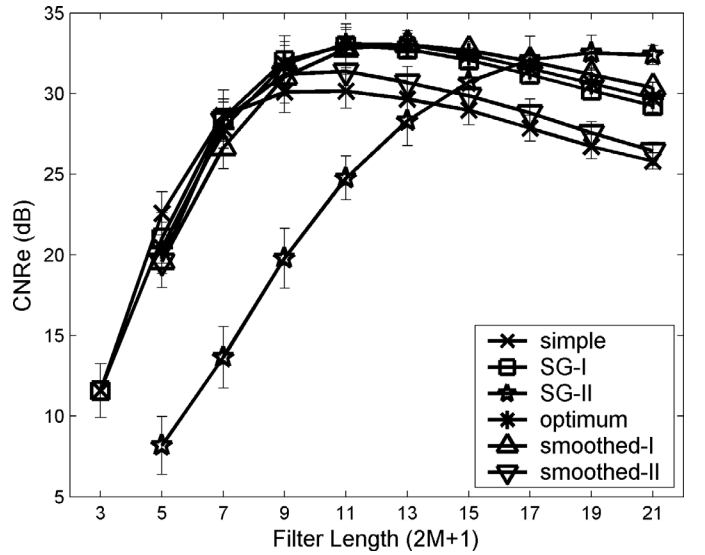


Fig. 8. The CNRes of the strain profiles obtained by various LPDDs. The window length is 2 mm at an overlap of 75%. The CNRe is calculated from a 1-D strain profile on the central line of the tissue and is plotted on a decibel (dB) scale. The results are averaged over 50 independent realizations; the error bars represent the standard deviations.

As shown in Fig. 8, the CNRes of all the LPDDs except for the SG-II DD have a similar behavior: they first increase with filter length, peak at a filter length of 11 or 13, and then decrease when the filter length increases further. For the SG-II DD, however, similar behavior is also expected if more data with longer filter lengths are plotted. At a low filter length, the CNRes of all the LPDDs but the SG-II DD are close, with the CNRe of the simple DD slightly better. At a long filter length, however, the CNRes of the optimum DD, the SG-I DD, and the smoothed-I DD are much higher than those of the simple DD and the smoothed-II DD. The SG-II DD has a much lower CNRe at low filter length, but reaches a CNR that is higher than that of any other LPDDs when the filter length is longer than 17.

D. Comparison of Axial Resolution

The ideal strain image of the double-lesion simulated tissue and the strain images calculated with various LPDDs are shown in Fig. 9. As evident from the figure, the rapid transitions (i.e., sharp corners) in the strain images are distorted by a long filter length LPDD. However, these sharp corners are better preserved by the SG-II DD. Based on the observations, it is expected that the SG-II DD will produce a strain image with a better axial resolution.

The axial resolution is an important parameter in elastographic performances. In our work, we used the definition of the axial resolution as the distance between the FWHMs of the strain profiles with two equally stiff lesions embedded in a softer homogenous background [21]. As shown in Fig. 10, the axial resolution is measured as the width between the two lesions indicated by the two arrows which point at half the calculated strain difference between the background and the lesions.

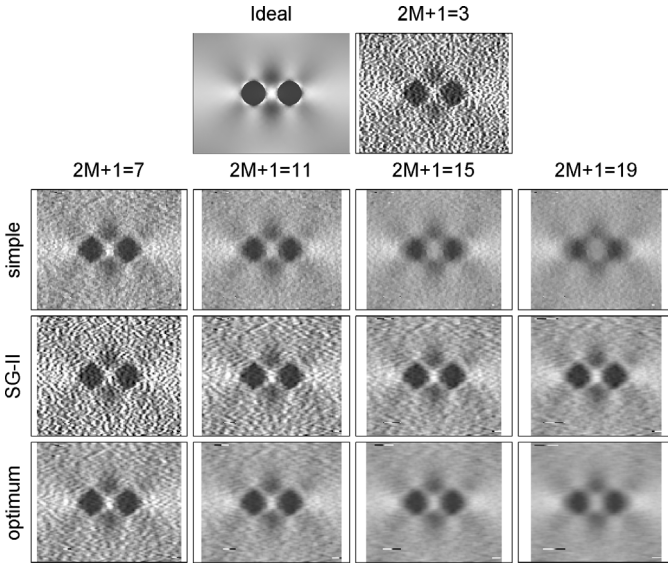


Fig. 9. The ideal axial strain image and strain images obtained by various LPDDs in the double-inclusion tissue model. All of the strain images are displayed with the same gray scale range of [0 0.020]. The horizontal axis denotes the axial direction (depth), while the vertical axis denotes the lateral direction (width).

The measurements of the axial resolution obtained by various LPDDs are shown in Fig. 11. The SG-II DD shows the best axial resolution. At a low filter length, the axial resolutions using other LPDDs are almost the same. At a long filter length, however, the axial resolutions using the smoothed-I DD, optimum DD, and the SG-I DD are slightly better than those using the simple DD and the smoothed-II DD.

IV. EXPERIMENTS

A. Phantom Experiments

Because of the lack of suitable elastographic phantoms, some raw RF data (A-lines) were borrowed from the University of Texas Medical School to validate the different performances of various LPDDs. The data have been used in [13]. They were obtained from a uniformly elastic phantom ($90 \times 90 \times 90 \text{ mm}^3$) with a cylindrical inclusion (7 mm radius) located roughly 40 mm below the top compressor plate. The phantom was compressed 1% axially. The details about the phantom and experimental settings are referred to [13]. The axial displacements were estimated using a window length of 2 mm and a window separation of 0.5 mm (i.e., at a 75% overlap).

B. In Vitro Experiments

Preliminary in vitro experiments on high-intensity focused ultrasound (HIFU)-induced lesion visualization [22], [23] are carried out in our work. The thermal lesion is induced in a piece of fresh excised ox liver with an approximate dimension of $60 \times 60 \times 60 \text{ mm}^3$. The operation is con-

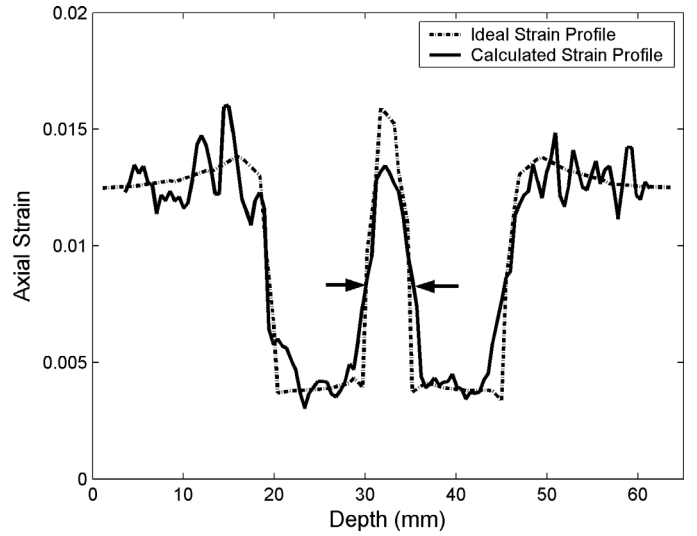


Fig. 10. Definition of the axial resolution measurement. The strain threshold indicated by the arrows represents half of the difference between the average calculated strain inside the lesions and the average calculated strain in the background tissue. The axial resolution is measured as the distance between the lesions where the calculated strains exceeded the threshold.

ducted by using an HIFU surgery system (JC, Chongqing Hifu Co., Ltd., Chongqing, China). Before the lesion induction, the liver is immersed in physiological saline solution. The air within the liver and the saline are pumped out by a mechanical pump in order to avoid ultrasonic attenuation. After lesion induction, the liver is immersed in the air-blood physiological saline solution again, and compressed by a flat compressor through a mechanical setting. The applied strain is approximately 1%.

A linear array transducer with 256 lines and a central frequency of 3.5 MHz (SJN2032, Haiying Co. Ltd., Wuxi, Jiangsu, China) is embedded in the compressor. The pre- and postcompression A-lines are acquired by a 12-bit AD card at a 20 MHz sampling frequency. The axial displacements are estimated using a window length of 2 mm and a window separation of 0.5 mm (i.e., at a 75% overlap).

V. RESULTS

Fig. 12 shows the sonography of the phantom and the corresponding strain images obtained by various LPDDs. Fig. 13 shows a photograph of the liver with an HIFU-induced lesion, and the strain images obtained by various LPDDs. As evident in Figs. 12 and 13, the elastographic performances of the phantom experiments and in vitro experiments, including the noise performances, contrast performances, and the axial resolution performances, are similar to the previous simulation results. As the filter length increases, the strain images are better smoothed, but at the expense of reduced contrast and axial resolution. The strain images obtained by the SG-II are the noisiest, but have the best axial resolution, especially at long filter length. The optimum DD and SG-II DD at a length of 11 or 15 appear to give the best overall performances.

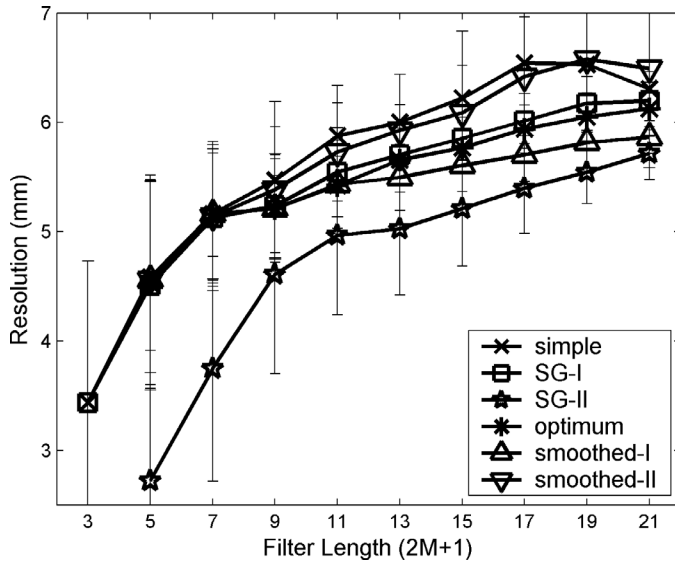


Fig. 11. The axial resolution measurement of the strain profiles obtained by various LPDDs. The window length is 2 mm at an overlap of 75%. The axial resolution is measured from a 1-D strain profile on the central line of the tissue. The results are the statistical means over 50 independent realizations; the error bars represent the standard deviations.

VI. DISCUSSION

The SNRe results in Fig. 5 are consistent to some extent with the minimum square error and the noise amplification factor of the LPDD in Figs. 1 and 3. As the filter length increases, the minimum square error and the noise amplification factor decrease, resulting in an improved SNRe in the axial strain calculation. In addition, the SG-I DD, the optimum DD, and the smoothed-I DD have the lowest minimum errors and noise amplification factors. Consequently, these three kinds of LPDDs have the best SNRes. In contrast, the SG-II DD has the highest minimum error and noise amplification factor. Accordingly, the corresponding SNRe is the worst. The superiority of the LSQSE method over the moving average filtering method [11] is again explained by the lower minimum square error and noise amplification factor of the SG-I DD as compared with those of the smoothed-II DD.

In practice, the trade-off between SNRe, CNRe, and axial resolution is inevitable [24], [25]. When applying an LPDD to axial strain calculation, high-frequency noises in the estimated displacements are largely eliminated. However, some small details of the strain profile are also distorted. Peaks are cut off, valleys are filled in, and rapid strain transitions (sharp corners) from the background to the lesion are flattened out. Finally, the contrast and resolution of the strain profile is reduced. From the viewpoint of digital signal processing, the small details of the strain profile may contribute to high-frequency components in the spectrum. Therefore, the decrease of the optimum cut-off frequency of the LPDD could result in the reduction of the contrast and the resolution. For example, the SG-II DD has the best axial resolution in the strain profile be-

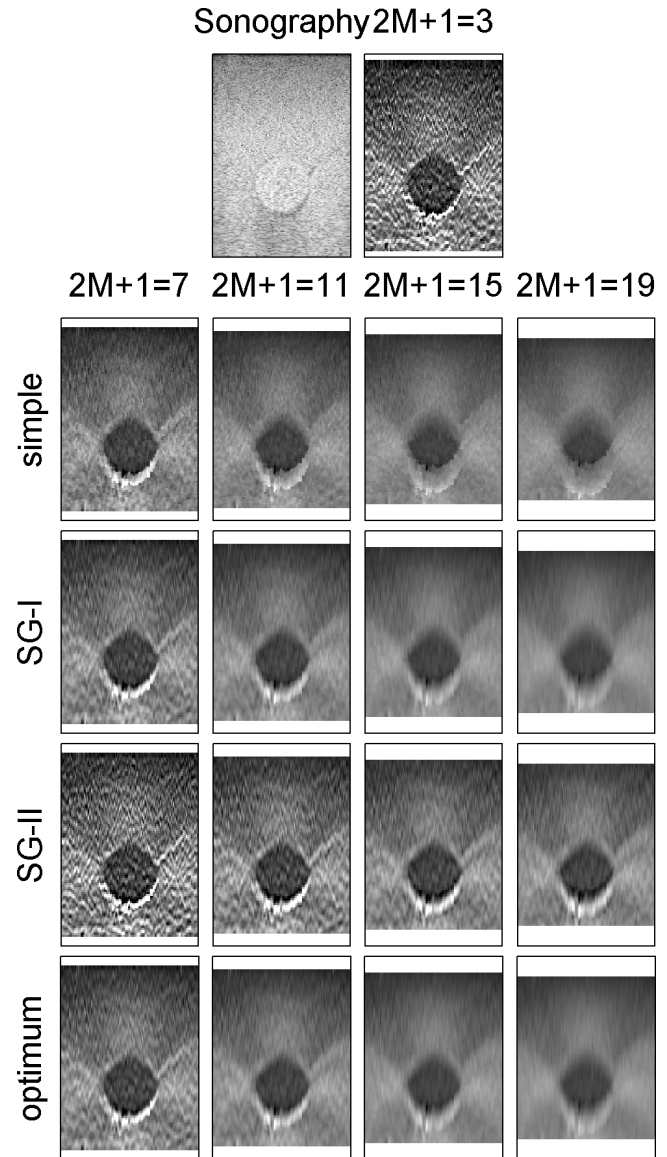


Fig. 12. Sonography of a $90 \times 90 \times 90 \text{ mm}^3$ gelatin phantom with a 10 mm radius cylindrical inclusion located at 40 mm below the transducer, and strain images obtained by various LPDDs. The sonography and the strain images correspond to a region of $57 \times 38 \text{ mm}^2$ (depth \times width). All of the strain images are displayed with the same gray scale range of $[0 \ 0.020]$. The horizontal axis denotes the lateral direction, while the vertical axis denotes the axial direction. The raw RF data (A-lines) were borrowed from the University of Texas Medical School and were used in [13]. See [13] for details.

cause its optimum cutoff frequency is the highest. As the filter increases, the optimum cutoff frequency decreases; and hence the axial resolution as well as the contrast are reduced.

The definition of the CNRe combines the noise with the contrast. At a low filter length, the increase of the CNRe is mainly related to the decrease of the strain deviation, i.e., the improvement of SNRe. With long filter lengths, the decrease of the CNRe is related to the decrease of the contrast. Therefore, there exists an optimum filter length with which the highest CNRe can be obtained. Since both the SNRe and the contrast results are consistent with the the-

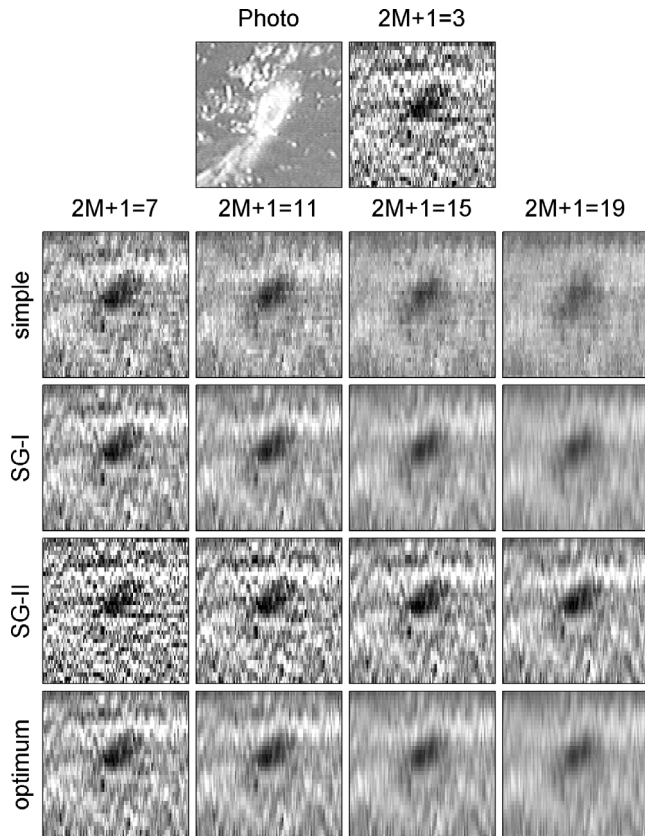


Fig. 13. A photograph of a HIFU-induced lesion and strain images obtained by various LPDDs. The photograph and the strain images correspond to a region of $40 \times 40 \text{ mm}^2$ near the HIFU-induced lesions. All of the strain images are displayed with the same gray scale range of $[0 \ 0.020]$. The horizontal axis denotes the lateral direction (width), while the vertical axis denotes the axial direction (depth). Note the axis difference between this figure and previous figures. The lack of correlation between the photograph and the strain images on the lesion outline is possibly because the photograph is not taken from exactly the ultrasonic scanning plane in the experiment.

oretical analysis of the LPDDs (i.e., the minimum square error, the optimum cutoff frequency and the noise amplification factor), the CNRe results also can be ultimately explained by the theoretical analysis. For example, the optimum cutoff frequency of the SG-II DD is the highest, and the contrast decreases the lowest. Therefore, the optimum filter length is the longest.

VII. CONCLUSION

Based on the results from this study, the SG-I DD, the optimum DD, and the smoothed-I DD are preferable for axial strain calculation in ultrasound elastography. If a long filter length is allowed, the SG-II DD can also be used to obtain a high CNRe and a small reduction of the axial resolution.

It can be expected that the elastographic performances of the LPDD as a function of the filter length depend on the window separation. For the simple DD, the effect of increasing the filter length is equivalent to that of increas-

ing the window separation. Since a large window separation normally results in an improved SNRe, the simple DD with a long filter length has an improved SNRe. In contrast, a small window separation (a high window overlap) increases the pixel number of strain images and thus improves the axial resolution [13]. Therefore, in order to balance the SNRe and the axial resolution as well as the CNRe, a small window separation and a long filter length are recommended.

ACKNOWLEDGMENTS

We gratefully acknowledge Prof. J. Ophir, Dr. S. Srinivasan, and Dr. R. Righetti, with the Department of Radiology, the University of Texas Medical School, for their kind assistance on the raw RF data of elastographic phantoms.

REFERENCES

- [1] J. Ophir, I. Céspedes, H. Ponnekanti, Y. Yazdi, and X. Li, "Elastography—a quantitative method for imaging the elasticity of biological tissues," *Ultrason. Imag.*, vol. 13, pp. 111–134, 1991.
- [2] M. O'Donnell, A. R. Skovoroda, B. M. Shapo, and S. Y. Emelianov, "Internal displacement and strain imaging using ultrasonic speckle tracking," *IEEE Trans. Ultrason., Ferroelect., Freq. Contr.*, vol. 41, pp. 314–325, 1994.
- [3] E. I. Céspedes, C. L. de Korte, and A. F. W. van der Steen, "Echo decorrelation from displacement gradients in elasticity and velocity estimation," *IEEE Trans. Ultrason., Ferroelect., Freq. Contr.*, vol. 46, pp. 791–801, 1999.
- [4] T. Varghese and J. Ophir, "Enhancement of echo-signal correlation in elastography using temporal stretching," *IEEE Trans. Ultrason., Ferroelect., Freq. Contr.*, vol. 44, pp. 173–180, 1997.
- [5] I. Céspedes and J. Ophir, "Reduction of image noise in elastography," *Ultrason. Imag.*, vol. 15, pp. 89–102, 1993.
- [6] T. Varghese, J. Ophir, and I. Céspedes, "Noise reduction in elastograms using temporal stretching with multicompression averaging," *Ultrasound Med. Biol.*, vol. 22, pp. 1043–1052, 1996.
- [7] S. J. Orfanidis, *Introduction to Signal Processing*. Englewood Cliffs, NJ: Prentice-Hall, 1996.
- [8] R. W. Hamming, *Digital Filters*. 3rd ed. Englewood Cliffs, NJ: Prentice-Hall, 1989.
- [9] S. Usui and I. Amidror, "Digital low-pass differentiation for biological signal processing," *IEEE Trans. Biomed. Eng.*, vol. BME-29, pp. 686–693, 1982.
- [10] A. E. Marble, C. M. McIntyre, R. Hastings-James, and C. W. Hor, "A comparison of algorithms used in computing the derivative of the left ventricular pressure," *IEEE Trans. Biomed. Eng.*, vol. BME-28, pp. 524–529, 1981.
- [11] F. Kallel and J. Ophir, "A least-squares strain estimator for elastography," *Ultrason. Imag.*, vol. 19, pp. 195–208, 1997.
- [12] K. M. Hiltawsky, M. Kruger, C. Starke, L. Heuser, H. Erment, and A. Jensen, "Freehand ultrasound elastography of breast lesions: Clinical results," *Ultrasound Med. Biol.*, vol. 27, pp. 1461–1469, 2001.
- [13] S. Srinivasan, J. Ophir, and S. K. Alam, "Elastographic imaging using staggered strain estimates," *Ultrason. Imag.*, vol. 24, pp. 229–245, 2002.
- [14] A. Savitzky and M. J. E. Golay, "Smoothing and differentiation of data by simplified least squares procedures," *Anal. Chem.*, vol. 36, pp. 1627–1639, 1964.
- [15] H. H. Madden, "Comments on the Savitzky-Golay convolution method for least-squares fit smoothing and differentiation of digital data," *Anal. Chem.*, vol. 50, pp. 1383–1386, 1978.
- [16] R. L. Burden and J. D. Faires, *Numerical Analysis*. 4th ed. Boston: PWS-Kent, 1989.

- [17] X. D. Zhang, *Modern Signal Processing*. 2nd ed. Beijing, China: Tsinghua University, 2002. (in Chinese)
- [18] R. L. Maurice and M. Bertrand, "Speckle-motion artifact under tissue shearing," *IEEE Trans. Ultrason., Ferroelect., Freq. Contr.*, vol. 46, pp. 584–594, 1999.
- [19] R. F. Wagner, S. W. Smith, J. M. Sandrik, and H. Lopez, "Statistics of speckle in ultrasound B-scans," *IEEE Trans. Sonics Ultrason.*, vol. 30, pp. 156–163, 1983.
- [20] M. Bilgen, "Target detectability in acoustic elastography," *IEEE Trans. Ultrason., Ferroelect., Freq. Contr.*, vol. 46, pp. 1128–1133, 1999.
- [21] R. Righetti, J. Ophir, and P. Ktonas, "Axial resolution in elastography," *Ultrasound Med. Biol.*, vol. 28, pp. 101–113, 2002.
- [22] F. Kallel, R. J. Stafford, R. E. Price, R. Righetti, J. Ophir, and J. D. Hazle, "The feasibility of elastographic visualization of HIFU-induced thermal lesions in soft tissues," *Ultrasound Med. Biol.*, vol. 25, pp. 641–647, 1999.
- [23] R. Righetti, F. Kallel, R. J. Stafford, R. E. Price, T. A. Krouskop, J. D. Hazle, and J. Ophir, "Elastographic characterization of HIFU-induced lesions in canine livers," *Ultrasound Med. Biol.*, vol. 25, pp. 1099–1113, 1999.
- [24] T. Varghese, J. Ophir, E. Konofagou, F. Kallel, and R. Righetti, "Tradeoffs in elastographic imaging," *Ultrason. Imag.*, vol. 23, pp. 216–248, 2001.
- [25] S. Srinivasan, R. Righetti, and J. Ophir, "Trade-offs between the axial resolution and the signal-to-noise ratio in elastography," *Ultrasound Med. Biol.*, vol. 29, pp. 847–866, 2003.



Jianwen Luo (S'02) was born in Fujian Province, China, in 1978. He received the B.S. degree in biomedical engineering from the Department of Electrical Engineering at Tsinghua University in 2000. He is currently pursuing the Ph.D. degree in the Department of Biomedical Engineering at the same university. His research interests include biomedical signal processing, ultrasound elastography and its application in high intensity focused ultrasound and radiofrequency ablation.



Jing Bai (M'87–M'90–SM'92–F'01) obtained the M.S. and Ph.D. degrees from Drexel University, Philadelphia, Pennsylvania, in 1983 and 1985. From 1985 to 1987 she was a research associate and an assistant professor with the Biomedical Engineering and Science Institute of Drexel University. In 1988, 1991, and 2000 she was an associate professor, professor, and Cheung Kong Chair Professor, respectively, in the Department of Electrical Engineering at Tsinghua University, Beijing, China. Currently she is with the Department of Biomedical Engineering at the same university.

Her research activities have included mathematical modeling and simulation of the cardiovascular system, optimization of cardiac assist devices, medical ultrasound, telemedicine, home health care network and home monitoring devices, and infrared imaging. She has published four books and over 100 journal papers.

She is a Fellow of IEEE. In 1997, she became associate editor of IEEE Transactions on Information Technology in Biomedicine.



Ping He (M'85–SM'97) was born in Shanghai, China, in 1945. He received the B.S. degree in physics from Fudan University, Shanghai, China, in 1968, and the M.S. and Ph.D. degrees in biomedical engineering from Drexel University, Philadelphia, Pennsylvania, in 1981 and 1984, respectively. From 1984 to 1985, he was a research fellow at Mayo Clinic, Rochester, Minnesota. In 1985, he joined the faculty of the Department of Biomedical, Industrial and Human Factors Engineering at Wright State University, Dayton, Ohio, and he is currently a Professor of Biomedical Engineering. Ping He is a senior member of the Institute of Electrical and Electronics Engineering, a member of Tau Beta Pi, and a registered Professional Engineer in Ohio.



Kui Ying received the B.S. and M.S. degrees in biomedical engineering from Tsinghua University, China, in 1987 and 1989, respectively, and the Ph.D. degree in electrical engineering and biomedical engineering from the Ohio State University, Ohio, in 1995. During her last year of graduate work, she started to work for Ford Motor Company and since then she has acquired over ten years of experience in software and business case analysis/design, and application development over several different industry companies in the United States, including Ford Motor Company, Abbott Laboratories, and IBM. In 2000, she and her family moved to Beijing, China, and she continued to work for IBM where she was involved in e-business projects. When at Tsinghua University, she was a student member of the IEEE and a member of the Engineering in Medicine and Biology Society of IEEE. While at Ford Motor Company, she was a member of the Society of Automotive Engineers (SAE). She is currently a research associate in the Biomedical Engineering Department at Tsinghua University. Her research interests include medical imaging, medical image processing, and computer simulations.